J. Biochem. 125, 495-506 (1999)

Resonance Assignments, Solution Structure, and Backbone Dynamics of the DNA- and RPA-Binding Domain of Human Repair Factor XPA[1]

Takahisa Ikegami,* Isao Kuraoka,† Masafumi Saijo,† Naohiko Kodo,† Yoshimasa Kyogoku,‡ Kosuke Morikawa,§ Kiyoji Tanaka,† and Masahiro Shirakawa*,[2]

*Graduate School of Biological Sciences, Nara Institute of Science and Technology, 8916-5 Takayama, Ikoma, Nara 630-0101; †Institute for Molecular and Cellular Biology, Osaka University, 1-3 Yamadaoka, Suita, Osaka 565-0871; ‡Institute for Protein Research, Osaka University, 3-2 Yamadaoka, Suita, Osaka 565-0871; and §Biomolecular Engineering Research Institute, 6-2-3 Furuedai, Suita, Osaka 565-0874

Received October 19, 1998; accepted November 26, 1998

XPA is involved in the damage recognition step of nucleotide excision repair (NER). XPA binds to other repair factors, and acts as a key element in NER complex formation. The central domain of human repair factor XPA (residues Met98 to Phe219) is responsible for the preferential binding to damaged DNA and to replication protein A (RPA). The domain consists of a zinc-containing subdomain with a compact globular structure and a C-terminal subdomain with a positively charged cleft in a novel α/β structure. The resonance assignments and backbone dynamics of the central domain of human XPA were studied by multidimensional heteronuclear NMR methods. ^{15}N relaxation data were obtained at two static magnetic fields, and analyzed by means of the model-free formalism under the assumption of isotropic or anisotropic rotational diffusion. In addition, exchange contributions were estimated by analysis of the spectral density function at zero frequency. The results show that the domain exhibits a rotational diffusion anisotropy ($D_{\parallel}/D_{\perp}$) of 1.38, and that most of the flexible regions exist on the DNA binding surface in the cleft in the C-terminal subdomain. This flexibility may be involved in the interactions of XPA with various kinds of damaged DNA.

Key words: NMR, nucleotide excision repair, relaxation, xeroderma pigmentosum, XPA.

Ultraviolet (UV) irradiation and some chemical agents produce alterations in DNA that are potentially mutagenic or lethal to cells. Usually, cells efficiently recognize and eliminate lesions through DNA repair processes. Nucleotide excision repair (NER) is the ubiquitous pathway by which a broad spectrum of structurally unrelated DNAs damaged by UV and chemical carcinogens is removed from the genome. The NER pathway repairs damaged DNA by recognizing lesions, excising the oligomer carrying the damaged bases, and synthesizing a repair patch using the opposite strand as a template (*1*). The importance of NER has been highlighted by studies on the human inherited disease, xeroderma pigmentosum (XP), which is characterized by a >1,000-fold higher frequency of skin cancers in sun-exposed areas, and by neurological complications (*2*). Cells from XP patients have defects in NER, and therefore are hypersensitive to UV irradiation. Complementation analyses have identified seven complementation groups (A-G) and a variant form in XP cells (*3*).

The gene that complements XP group A cells encodes a zinc-finger protein, XPA, composed of 273 amino acids. XPA has been shown *in vitro* to bind preferentially to various kinds of DNA damage such as (6-4) photoproducts and crosslinks caused by UV and chemical carcinogens. It has, therefore, been suggested that XPA is involved in the damage verification and/or recognition step of NER (*4-8*). XPA has also been shown to bind directly to other repair factors: replication protein A (RPA), ERCC1 (excision repair cross-complementing rodent repair deficiency 1)/XPF heterodimer, and TFIIH (transcription factor II H), which contains XPB and XPD as its subunits (*9-16*). All of these factors are essential for the early steps of NER (*1, 17*). *In vitro* experiments have shown that XPA has a moderately higher affinity for damaged DNA over undamaged DNA, and exhibits considerably enhanced preferential binding in the presence of RPA (*9, 10*). It was also shown that the binding activity of XPA to damaged DNA is increased by the interaction of XPA with ERCC1 (*16*). Thus, it has been suggested that XPA plays a role in loading the incision protein complex onto a damaged site as a multifunctional protein that coordinates the early steps of NER processes (*11, 13*). Recently, it has also been reported that XPA, RPA, TFIIH, XPC-HHR23B, XPG, and ATP are required for high specificity DNA-protein complex formation (*18*). There has been another suggestion of a two-step

---

[1] This work was supported by grants to T.I., M.S., and K.T. from the Ministry of Education, Science, Sports and Culture of Japan. M.S. was also supported by the Ciba-Geigy (Japan) Foundation for the Promotion of Science. This work was partly supported by a research grant to K.T. and K.M. from the Human Frontier Science Program.

[2] To whom correspondence should be addressed. Phone: +81-743-72-5571, Fax: +81-743-72-5579, E-mail: shira@bs.aist-nara.ac.jp

Abbreviations: CPMG, Carr-Purcell-Meiboom-Gill; ERCC1, excision repair cross-complementing rodent repair deficiency 1; HSQC, heteronuclear single quantum correlation; NER, nucleotide excision repair; NOE, nuclear Overhauser effect; RPA, replication protein A; TFIIH, transcription factor II H; XP, xeroderma pigmentosum.

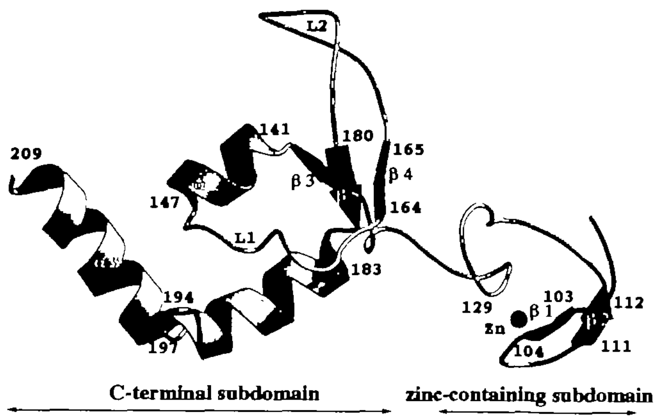

Fig. 1. **A ribbon diagram of the solution structure of the central domain of human XPA.** The domain consists of a zinc-containing subdomain (residues 102 to 129) and a C-terminal subdomain (residues 138 to 209), connected by an eight amino acid linker sequence (PDB: 1xpa) (*22*). Secondary structure elements are helices $\alpha1$ (residues 141 to 147), $\alpha2$ (residues 183 to 194), and $\alpha3$ (residues 197 to 209), strands $\beta1$ (residues 103 to 104), $\beta2$ (residues 111 to 112), $\beta3$ (residues 139 to 140), $\beta4$ (residues 164 to 165), and $\beta5$ (residues 180 to 181), and loops L1 (residues 148 to 163) and L2 (residues 166 to 179). The C-terminal sequence (residues 211 to 219) was excluded from the structure calculations (*22*). The figure was drawn with the programs, MOLSCRIPT (*52*) and RASTER3D (*53*).

mechanism for damage recognition in which damage is detected by XPC-HHR23B and then verified by XPA (*19*).

XPA consists of several distinct functional domains. Its amino (N)-terminal part contains a region (residues 4 to 74) for binding to a subunit of RPA, RPA34, and a region (residues 59 to 97) for binding to ERCC1 (*11, 12, 14–16*). The carboxyl(C)-terminal part of XPA, residues 226 to 273, has been shown to bind to TFIIH and recruit it to the damaged site (*12, 13*). The central domain (residues Met98 to Phe219), designated MF122 by Kuraoka *et al.*, has been identified as the minimal polypeptide essential for the preferential binding to damaged DNA by means of a combination of limited proteolysis and deletion analysis (*8*). The central domain also includes a region essential for binding to RPA70 (*10, 11*).

The central domain contains the zinc-binding sequence, Cys-X-X-Cys-$(X)_{17}$-Cys-X-X-Cys, in its N-terminal part (*20*). ^{113}Cd-NMR analysis combined with site-directed mutagenesis and atomic absorption have shown that one zinc ion is tetrahedrally coordinated by four Cys residues in the zinc-binding sequence (*20*). Miyamoto *et al.* have shown that a mutation at each of the four zinc-coordinating Cys residues results in a drastic reduction in the UV resistance of cells, as compared to the wild-type XPA protein (*21*). However, a mutation at Cys153, which is located outside of the zinc-binding sequence, gives almost the same UV resistance as that of the wild-type XPA. These results indicate that XPA has a $(Cys)_4$ type zinc-finger motif. It was generally thought that the zinc-finger motif of XPA was involved in DNA binding, through analogy to the zinc-finger motifs found in transcriptional regulatory factors.

Recently, in a short communication, we reported the structure of the central domain of human XPA determined by NMR and its interactions with damaged DNA and RPA70 (*22*). The central domain consists of a zinc-containing subdomain, a C-terminal subdomain with a positively charged cleft, and a linker sequence that connects these two subdomains (Fig. 1). By analyzing the spectra of its complex with a cisplatin-damaged oligonucleotide or a truncated RPA70, we found that the cleft in the C-terminal subdomain serves as the DNA-binding surface and that the zinc-containing subdomain serves as an RPA70-binding surface. Recently, another group has also reported the backbone assignments (*23*) and structural features (*24, 25*) of this domain of XPA.

Here, we present resonance assignments of the backbone and sidechain ^{1}H, ^{15}N, and ^{13}C nuclei, and backbone dynamics of the central domain of human XPA. We investigated the backbone dynamics by analyzing the ^{15}N T_1, T_2, and NOE (nuclear Overhauser effect) relaxation data obtained by NMR at two static magnetic fields. From the results, we have found the anisotropic character of the rotational diffusion of the central domain. The DNA binding surface appears highly dynamic, suggesting possible relationships to the versatility of the damage recognition of XPA. We also compared the dynamic parameters obtained on model-free analyses under the assumptions of isotropic rotational diffusion and anisotropic rotational diffusion.

MATERIALS AND METHODS

Sample Preparation—The central domain of human XPA, XPA$_{98\text{-}219}$, was expressed in BL21(DE3) strain *Escherichia coli* cells transformed with vector plasmids containing the gene under the control of the phage T7 promoter. For NMR experiments, uniformly ^{15}N- or ^{15}N-, ^{13}C-labeled XPA$_{98\text{-}219}$ were produced by growing the *E. coli* in M9 medium containing 0.5 g/liter $^{15}NH_4Cl$, without or with 1.0 g/liter [*U*-^{13}C]glucose, respectively. A uniformly ^{15}N-labeled and fractionally deuterated XPA$_{98\text{-}219}$ (C153S) point mutant (*20*) was also prepared by growing the *E. coli* in the presence of 80% ^2H_2O. The recombinant proteins were purified by SP-Sepharose (Pharmacia) and Mono-S (Pharmacia) ion-exchange and Sephacryl S-100 (Pharmacia) gel-filtration chromatographies. Samples for NMR measurements typically comprised 1.2 mM protein in 50 mM deuterated Tris-HCl (pH 7.3 at 30°C), 150 mM KCl, 10 mM DTT, and 20 μM $Zn(CH_3COO)_2$ in 90% H_2O/10% ^2H_2O.

NMR Spectroscopy for Resonance Assignments and Structure Analysis—All NMR spectra for resonance assignments were acquired at 30°C with a Bruker DMX500 or DRX500 NMR spectrometer. For the assignments of the ^{1}H, ^{15}N, and ^{13}C resonances, a series of three-dimensional experiments [^{15}N-edited NOESY, ^{15}N-edited TOCSY, HNCA, HNCO, HN(CA)CO, CBCA(CO)NH, CBCANH, HN(CA)HA, HBHA(CBCACO)NH, HBHA(CBCA)NH, C(CO)NH, H(CCO)NH, and HCCH-TOCSY] were performed with the ^{15}N- or ^{15}N,^{13}C-labeled protein dissolved in 90% H_2O/10% ^2H_2O (*26, 27*). A HCCH-TOCSY spectrum was also acquired with a sample dissolved in 99.8% ^2H_2O. Stereospecific assignments of the methyl groups of the Leu and Val residues were achieved with a 15% fractionally ^{13}C-labeled protein dissolved in 99.8% ^2H_2O as described (*28*).

Interproton distance information was obtained from 2D, ^{15}N- or ^{13}C-edited 3D, or ^{13}C,^{15}N- or ^{13}C,^{13}C-edited 4D

NOESY spectra acquired at 30°C with a Bruker DRX500 or DRX800 NMR spectrometer with a mixing time of 100 ms (*26*). In addition, 14 restraints were obtained through a ^{15}N,^{15}N-edited 4D NOESY experiment on the uniformly ^{15}N-labeled and fractionally deuterated XPA$_{98\text{-}219}$ (C153S) mutant, since the mutant was shown to have a conformation identical to that of the wild type XPA$_{98\text{-}219}$ based on the (^{15}N, ^{1}H) heteronuclear single quantum correlation (HSQC) and ^{113}Cd-NMR spectra (*20*). HMQC-J and HNHA spectra were measured to obtain the backbone vicinal coupling constants ($^{3}J_{\mathrm{HN,H}\alpha}$), and the data were used for torsion angle constraints (*26, 27*).

Amide proton exchange with solvent was monitored by means of a series of ^{15}N-^{1}H-HSQC spectra after dissolving lyophilized ^{15}N-labeled XPA$_{98\text{-}219}$ in ^{2}H$_2$O to a final concentration of 0.58 mM. The spectra were recorded every 30 min at pH 6.5 at 30°C. The signals remaining after exchange were identified.

Measurements of ^{15}N T_1, T_2, and NOE—Spectra for ^{15}N spin-lattice relaxation times, T_1, ^{15}N spin-spin relaxation times, T_2, and {^{1}H}-^{15}N steady-state heteronuclear NOE values were acquired at 30°C with Bruker DRX500 and DRX800 spectrometers, equipped with pulsed field gradient probes, operated at ^{15}N frequencies of 50.7 and 81.1 MHz, respectively. The enhanced-sensitivity pulse sequences used for these experiments were described previously (*29*). The T_1 relaxation delays were 5, 65, 145, 245, 365, 525, 755, and 1,145 ms at 50.7 MHz, and 5, 105, 215, 355, 525, 735, 1,035, 1,555, and 2,000 ms at 81.1 MHz. The T_2 relaxation delays were 14.4, 28.8, 43.2, 57.6, 72.0, 100.8, and 144.0 ms at 50.7 MHz, and 7.2, 14.4, 28.8, 43.2, 57.6, 79.2, 108.0, and 151.2 ms at 81.1 MHz. The delay between ^{15}N 180° pulses in the Carr-Purcell-Meiboom-Gill (CPMG) sequence for the T_2 measurements was 900 μs. In the experiments for {^{1}H}-^{15}N steady-state NOE, relaxation delays of 3.6 and 1.6 s before the ^{1}H saturations of 3.0 and 5.0 s were applied at 50.7 and 81.1 MHz, respectively. The ^{1}H saturations were achieved with 120° ^{1}H pulses applied every 5 ms. The spectral widths were 6,009.615 (^{1}H) and 810.938 Hz (^{15}N) at 50.7 MHz, and 13,020.833 (^{1}H) and 1,297.387 Hz (^{15}N) at 81.1 MHz. The ^{1}H carrier was set to the frequency of the water resonance (4.7 ppm), and the ^{15}N carrier was set to 119.4 ppm. For the T_1 and T_2 measurements, 512 (^{1}H)×200 (^{15}N) and 1,024 (^{1}H)×200 (^{15}N) complex points of 32 scans were collected at 50.7 and 81.1 MHz, respectively. For the {^{1}H}-^{15}N NOE measurements, 512 (^{1}H)×200 (^{15}N) and 1,024 (^{1}H)×128 (^{15}N) complex points of 64 scans were collected at 50.7 and 81.1 MHz, respectively. All data sets were processed with the program, NMRPIPE (*30*). Lorentz-to-Gauss transformations were applied to both ^{1}H and ^{15}N dimensions.

Estimation of ^{15}N T_1, T_2, and NOE—Peak heights were determined from the spectra using the program package, PIPP (*31*). The root mean square (r.m.s.) value of the background noise of each spectrum was used as uncertainties of the measured intensities. Each T_1 and T_2 value was determined by fitting a series of measured intensities to a two-parameter function of the form, $I(t)=I_0\exp(-t/T_{1,2})$, where $I(t)$ is the intensity after a time delay t, and I_0 is the intensity at time zero. Nonlinear least-square fitting according to the Levenberg-Marquardt method was employed for optimization of the values of the I_0 and $T_{1,2}$ parameters using the program, CURVEFIT (*32*). Only results with χ^2 values smaller than the tabulated χ^2 values at the 95% confidence level were used, where χ^2 equals $\Sigma\{I_c(t)-I_e(t)\}^2/\sigma_i^2$ [$I_c(t)$: the intensity calculated from the fitting parameter values, $I_e(t)$: the experimental intensity, σ_i: the uncertainty of the experimental value], and summation was performed on the available experimental data set. The uncertainties of the $T_{1,2}$ values were estimated from the Levenberg-Marquardt error matrices (*33*). The {^{1}H}-^{15}N steady-state NOE values were determined from the ratios of the intensities of the peaks with and without proton saturation. The uncertainties of the NOE values were estimated according to the error propagation equation (*33*).

Estimation of Effective J(0) Spectral Density Functions and Chemical Exchange Rates, R_{ex}—The effective spectral density function at zero-frequency, $J_{eff}(0)$, is defined as the sum of inherent $J(0)$ and a chemical exchange term. The $J_{eff}(0)$ values for the backbone ^{15}N nuclei were calculated from the ^{15}N T_1, T_2, and NOE values according to the following equation (*34, 35*):

$$\begin{aligned} J_{eff}(0) &= J(0)+\lambda R_{ex} \\ &= \lambda\,[-1/(2T_1)+1/T_2-3\gamma_N\ (\mathrm{NOE}-1)/(5\gamma_H T_1)], \end{aligned}$$

where $\lambda=3/(6d+2c)$, $d=\gamma_H^2\gamma_N^2\ (h/2\pi)^2/(4r_{HN}^6)$, and $c=\Delta^2\omega_N^2/3$; Δ is the chemical shift anisotropy of the amide ^{15}N nucleus (−160 ppm); ω_N is the angular resonance frequency of the ^{15}N nucleus; γ_H and γ_N are gyromagnetic ratios for the ^{1}H and ^{15}N nuclei, respectively; h is Planck's constant; and r_{HN} is the length of the amide ^{15}N-^{1}H bond (1.02 Å). The λ values calculated at 50.7 MHz ($\lambda_{50.7}$) and 81.1 MHz ($\lambda_{81.1}$) are approximately 0.787×10^{-9} and 0.613×10^{-9} (s^2/rad), respectively. The chemical exchange rate, R_{ex}, was calculated from the $J_{eff}(0)$ values obtained at 50.7 MHz [$J_{eff}(0)_{50.7}$] and 81.1 MHz [$J_{eff}(0)_{81.1}$] according to the following equation (*34, 35*):

$$\begin{aligned} R_{ex}\ (\text{at }\omega_N) = \omega_N^2\ [J_{eff}(0)_{81.1}-J_{eff}(0)_{50.7}]/ \\ (\lambda_{81.1}\ \omega_{N81.1}^2-\lambda_{50.7}\ \omega_{N50.7}^2). \end{aligned}$$

The uncertainties of the $J_{eff}(0)$ and R_{ex} values were estimated from the uncertainties of the ^{15}N T_1, T_2, and NOE values according to the error propagation equation (*33*).

Model-Free Analysis with an Isotropic Rotational Diffusion Model—An initial estimate of the overall rotational correlation time, τ_m, was obtained from the average T_1/T_2 ratios at 50.7 MHz, which were limited to within one σ (SD). In the model-free analysis developed by Lipari and Szabo (*36, 37*) with the assumed isotropic rotational diffusion model, the following five dynamic models were applied according to Mandel *et al.* (*32*). The models and the combinations of optimized parameters were (1) S^2, (2) S^2 and τ_{ef}, (3) S^2 and R_{ex}, (4) S^2, τ_{ef} and R_{ex}, and (5) S_f^2, S^2 and τ_{es}, where S^2 is the square of the order parameter, τ_e is the effective correlation time, R_{ex} is the chemical exchange rate, and subscripts f and s indicate fast and slow time scales, respectively. In model 5, the extended formula of the spectral density function was used (*38*). For residues for which the ^{15}N relaxation data were available at both 50.7 and 81.1 MHz, model-free analyses were performed by fitting the data for the two fields simultaneously with the assumed quadratic field dependence of the exchange contribution to the ^{15}N transverse relaxation rate ($1/T_2$). Otherwise, the analyses were performed by fitting only the available data. First, the data were fitted to each of the five dynamic models with the overall rotational correlation time, τ_m, fixed at the initially estimated value. Then, one of the dynamic models was statistically selected for each backbone ^{15}N spin by means of Monte Carlo numerical simulations and F-statistical tests as described by Mandel *et al.* (*32*). Finally, τ_m and the internal motion parameters were simultaneously optimized with the selected dynamic models. The uncertainty for each parameter was estimated by means of a Monte Carlo simulation. All analyses were performed using the program, MODELFREE-4.0 (*32*).

Model-Free Analysis with an Anisotropic Rotational Diffusion Model—The magnitude and orientation of the anisotropic rotational diffusion tensor, *D*, were estimated from the T_1/T_2 ratios and the molecular coordinates of the central domain of XPA. Thirty amide groups were excluded as these have significant internal motions manifested by {^{1}H}-^{15}N steady-state NOE values of less than 0.65 or large exchange rates manifested by R_{ex} values estimated by $J(0)$ analysis at larger than 2.5 s^{-1} at 50.7 MHz. The structure showing the lowest backbone r.m.s.d. from the mean of the final 30 structures calculated through the simulated annealing procedure was used for the analysis (*22*) (PDB: 1xpa). The axially symmetric diffusion tensor was calculated with the program, R2_R1_DIFFUSION, in the package, MODELFREE-4.0 (*32*), and the fully anisotropic diffusion tensor was calculated using an in-house program. In the analyses, the experimentally obtained T_1/T_2 ratios were fitted to an anisotropic diffusion model by means of non-linear optimization procedures to obtain the best fits with the T_1/T_2 ratios predicted from the fittings (*39*). Based on the estimated magnitude and orientation of the anisotropic rotational diffusion tensor, *D*, model-free analysis with the axially symmetric anisotropic diffusion model was performed. The procedure was essentially the same as that employed in the analysis with the isotropic diffusion model except for the following points. First, the diffusion tensor, *D*, was used instead of the single overall rotational correlation time, τ_m. Second, the extended expression of the spectral density function (model 5) was not used in the model selection procedure. Third, the information regarding the orientations of the amide NH bond vectors obtained from the molecular coordinates was used. Last, the spectral density function for an axially symmetric diffusion model (*39, 40*) was applied.

RESULTS

Resonance Assignments—The resonance assignments for the backbone nuclei were completed except those of residues 98, 99, 131, 152, 153, and 170-174. The ^{15}N/^{1}H signals of the backbone amides of these residues, except Pro170, could not be observed, probably due to conformational averaging or hydrogen exchange with the solvent. Most of the side-chain resonances were assigned except those of residues 151, 152, and 170-173. All the methyl groups on the twelve Leu and five Val residues were assigned stereospecifically with a 15% fractionally ^{13}C-labeled protein. The average values of the backbone vicinal coupling constants ($^3J_{HN,H\alpha}$) estimated from HMQC-J and HNHA spectra were used for torsion angle constraints. Figure 2 shows the sequential NOE connectivities, amide

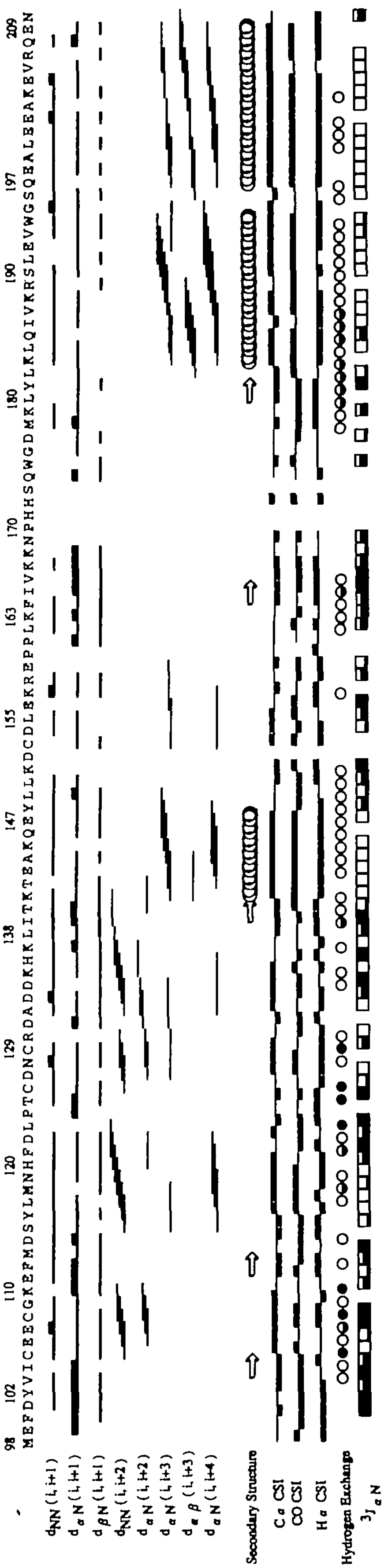

Fig. 2. **Summary of the sequential and medium-range NOE connectivities, secondary structures, chemical shift indexes, amide hydrogen exchange data, and $^3J_{HN,H\alpha}$ coupling constants observed for the central domain of human XPA.** The NOE connectivities are represented by bars, the size of which indicates the NOE intensity (strong or weak). The notation $d_{\alpha N}(i,i+1)$, for example, shows the connectivity between the α proton resonance of an amino acid and the amide proton resonance of the next amino acid in the sequence. Amide protons that exchanged slowly at pH 6.5 at 30°C are indicated. (Open circles) Life times longer than 30 min and shorter than 2 h. (Half filled circles) Life times longer than 2 h and shorter than 10 h. (Filled circles) Life times longer than 10 h. Three-bond scalar coupling constants between spins H_N and H_α ($^3J_{\alpha N}$) smaller than 4 Hz are indicated by open boxes, those larger than 4 Hz and smaller than 6 Hz are indicated by one-third filled boxes, those larger than 6 Hz and smaller than 8 Hz are indicated by two-thirds filled boxes, and those larger than 8 Hz are indicated by filled boxes. The chemical shift indexes (CSI) are plotted for ^{13}C$_\alpha$, ^{1}H$_\alpha$, and ^{13}C' resonances (*41*). Upper bars represent +1, lower bars −1, and horizontal lines 0. The figure was produced with the program, VINCE (1996, Rowland Institute for Science).

proton exchanges, ${}^3J_{HN,H\alpha}$ coupling constants, and chemical shift indexes (CSI) for ${}^{13}C_\alpha$, ${}^1H_\alpha$, and ${}^{13}C'$ resonances (*41*).

${}^{15}N$ Relaxation Data—The relaxation data, ${}^{15}N$ T_1, T_2, {${}^1H$}-${}^{15}N$ steady-state NOE, and T_1/T_2 ratios, were obtained by analysis of the ${}^1H$-detected ${}^{15}N$-${}^1H$ correlation spectra of $XPA_{98\text{-}219}$ at 50.7 and 81.1 MHz ${}^{15}N$ frequency fields (Fig. 3). Most data for the ${}^{15}N$ spins in the five N-terminal residues (98 to 102), the five residues (170 to 174) in loop L2, and the four C-terminal residues (216 to 219) could not be obtained due to signal broadening or severe signal overlapping in the spectra. Smaller {${}^1H$}-${}^{15}N$ NOE values (<0.55 at 50.7 MHz) were found for a part of loop L1 (residue 158), most of loop L2 (residues 168 to 179, except for non-detectable resonances), and the latter part of helix $\alpha3$ (residues 206 to 209); markedly smaller or negative {${}^1H$}-${}^{15}N$ NOE values (<0.2 at 50.7 MHz) were found for the N-terminal region (residue 102) and the C-terminal region (residues 212 to 218, except for non-detectable resonances). The T_1/T_2 ratios showed wide distribution ranges [$10.8\pm2.2(1\sigma)$ at 50.7 MHz and $25.9\pm7.7(1\sigma)$ at 81.1 MHz], implying the presence of anisotropy in the rotational diffusion of the domain.

J(0) Analysis—The effective spectral density function at zero-frequency, $J_{eff}(0)$, is defined as the sum of $J(0)$ and λR_{ex} (*34*). Because R_{ex} values are proportional to the square of the magnetic field strength, and $J(0)$ values are independent of the field strength, R_{ex} values can be determined from $J_{eff}(0)$ values obtained at two different field strengths. Figure 4 shows the $J_{eff}(0)$ values at 50.7 and 81.1 MHz, and the calculated R_{ex} values. The mean and SD of the R_{ex} values at 50.7 MHz was $1.54\pm0.97\ s^{-1}$. High R_{ex} values ($>3.5\ s^{-1}$ at 50.7 MHz) were found for residues 133 and 134 in the linker sequence, and residues 154 and 156 in loop L1.

Comparison of Isotropic, Axial Symmetric, Fully Anisotropic Models—To determine which diffusion model is more appropriate for the analysis of the relaxation data, the experimental T_1/T_2 ratios were fitted to each of the isotropic, axially symmetric, and fully anisotropic diffusion models. The results of the fitting were evaluated by means of F-statistical tests (*39*). The T_1/T_2 ratios at 50.7 MHz were used for the analysis since they were expected to involve less contribution from the chemical exchange rates, R_{ex}, than those at 81.1 MHz. The T_1/T_2 ratios of residues whose {${}^1H$}-${}^{15}N$ NOE values were smaller than 0.65 at 50.7 MHz, or whose R_{ex} values were greater than 2.5 s^{-1} on $J(0)$ analysis were excluded from the analysis. χ^2 values, 320.0, 194.3, and 182.9, were obtained for the isotropic, axially symmetric, and fully anisotropic diffusion models, respectively. For these χ^2 values, the F-statistical values were calculated to be 11.9 between the isotropic and axially symmetric models, and 1.7 between the axially symmetric and fully anisotropic models. These F-statistical values were used to determine whether the improvement in the fitting, expressed as the χ^2 values, made by using a more complicated model is significant or merely arises due to the

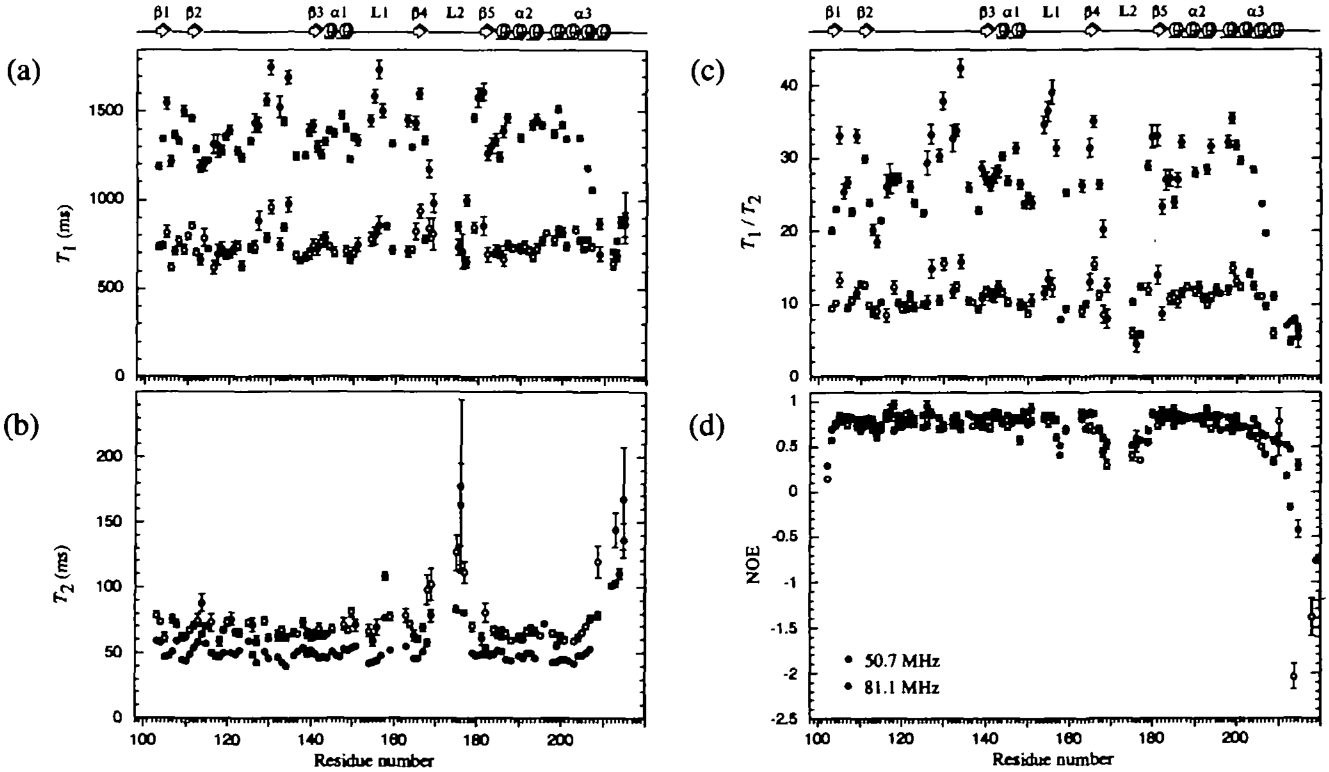

Fig. 3. **Plots of amide ${}^{15}N$ T_1, T_2, T_1/T_2, and NOE against residue numbers.** The data were measured at ${}^{15}N$ frequencies of 50.7 MHz (open circles) and 81.1 MHz (filled circles). (a) Longitudinal relaxation times, T_1. (b) Transverse relaxation times, T_2. (c) T_1/T_2 ratios. (d) Heteronuclear {${}^1H$}-${}^{15}N$ steady-state NOE values defined as I/I_0, where I and I_0 are the intensities of the peaks with and without ${}^1H$ saturation, respectively. For plots a-d, the error bars indicate the ±SD (1σ) values of the uncertainties of the data. The secondary structures are indicated at the top.

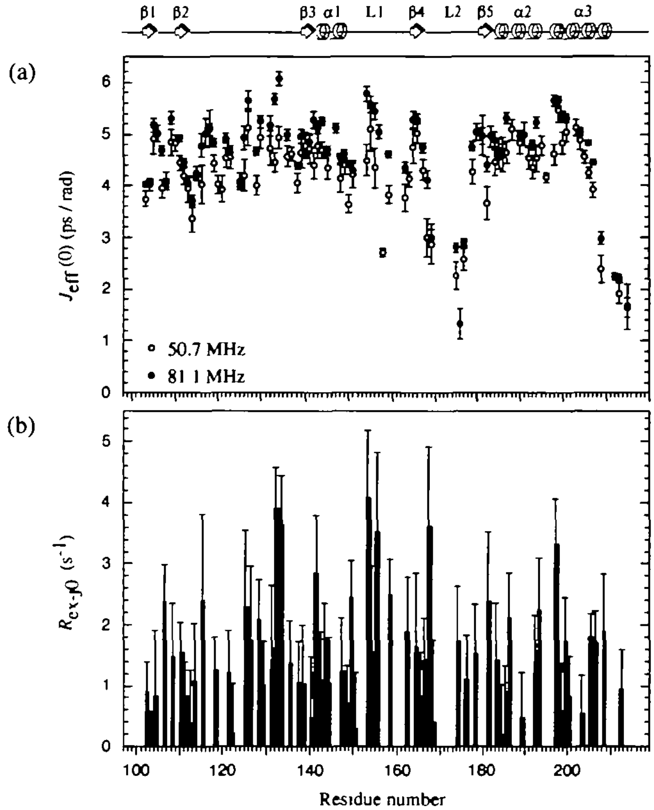

Fig. 4. **Plots of the results of $J(0)$ analysis against residue numbers.** (a) Reduced effective spectral density functions at zero frequency, $J_{\rm eff}(0)$, estimated at ^{15}N frequencies of 50.7 MHz (open circles) and 81.1 MHz (filled circles). (b) Chemical exchange rates, $R_{\rm ex\text{-}J0}$, were calculated from the $J_{\rm eff}(0)$ values estimated at the two static magnetic fields. For plots a and b, the error bars indicate the ±SD (1σ) values of the uncertainties of the data. The secondary structures are indicated at the top.

incorporation of additional parameters that causes a reduction in the degrees of freedom (*32*). The F-statistical value for the isotropic and axially symmetric models (11.9) was significantly larger than the corresponding tabulated 95% critical value of 2.8 obtained from the statistical table presented by Bevington and Robinson (*33*). On the other hand, that for the axially symmetric and fully anisotropic models (1.7) was smaller than the corresponding tabulated 95% critical value of 3.2. These results show that the improvement in the fitting made by using the axially symmetric diffusion model instead of the isotropic model is statistically significant, but that made by using the fully anisotropic model instead of the axially symmetric model arises merely due to the incorporation of additional parameters.

Another test of the validity of the axially symmetric model was performed using in-house programs. First, the T_1/T_2 ratios at 50.7 MHz were randomly assigned to the 59 backbone amide bond vectors in XPA. This random assignment removes the correlation between the orientations of the amide bond vectors and the T_1/T_2 ratios (*39*). Then, an axially symmetric model was used for the fitting to these randomly assigned T_1/T_2 ratios. The procedures for the random assignment and the fitting to these data were independently repeated 200 times, and then the statistical significance was evaluated. The average and minimum values of χ^2 obtained through the 200 simulations were 299.8 and 242.1, respectively. As the value of χ^2, 194.3, for the fitting based on the correct amide bond vectors was smaller than the minimum χ^2 value of 242.1 in the 200 random simulations, the correlation between the T_1/T_2 values and the orientations of the amide bond vectors is statistically significant.

Model-Free Analyses—The relaxation data were analyzed by means of model-free formalism under the assumption of isotropic rotational diffusion, or the assumption of axially symmetric anisotropic rotational diffusion. The results were compared to determine which model was more appropriate, *i.e.*, the isotropic diffusion model or the axially symmetric anisotropic diffusion model.

Initial Estimation of the Overall Correlation Time and Rotational Diffusion Tensor—The overall rotational correlation time, $\tau_{\rm m}$, estimated from the mean (10.81 ± 0.65 [uncertainty]) of the 61 one σ trimmed T_1/T_2 ratios at 50.7 MHz was 12.13 ± 0.43 ns. The number of spins for which the {^{1}H}-^{15}N NOE values were smaller than 0.65 at 50.7 MHz was 23, and the number of spins for which the $R_{\rm ex}$ values estimated on $J(0)$ analysis were larger than 2.5 s^{-1} at 50.7 MHz was seven. These spins were excluded from the calculation of the axially symmetric rotational diffusion tensor, D. The remaining 59 T_1/T_2 ratios at 50.7 MHz and the coordinates of XPA (PDB: 1xpa) were used to estimate the principal values of the tensor. The ratio of the diffusion constants parallel and perpendicular to the long axis of the symmetric rotor ($D_{\parallel}/D_{\perp}$) was 1.38 ± 0.04, and the average correlation time ($1/[2D_{\parallel}+4D_{\perp}]$) was 12.03 ± 0.05 ns (Fig. 5). The orientations of the unique axes of the calculated diffusion tensor and the inertia moment estimated only from the molecular coordinates agreed well (7.9° difference).

Selection of the Dynamic Models—The experimental ^{15}N T_1, T_2, and NOE values were fitted to dynamic models 1 to 5 with the isotropic diffusion model with $\tau_{\rm m}$ fixed at the initially estimated value, 12.13 ns, using a statistical model selection protocol (*32*). Likewise, the values were fitted to dynamic models 1 to 4 with the axially symmetric diffusion model with a fixed orientation and magnitude of the diffusion tensor, D. Table I summarizes the number of spins for which each dynamic model was selected. One of the two simpler models, 1 or 2, was chosen for 15 spins with the isotropic model, while one of them was chosen for 28 spins with the anisotropic model, suggesting that the anisotropic diffusion model is more appropriate than the isotropic model for model-free analysis.

Optimization of $\tau_{\rm m}$, D, and Internal Motion Parameters—The overall rotational correlation time, $\tau_{\rm m}$, for the isotropic diffusion model or the diffusion tensor, D, for the anisotropic diffusion model, and the internal motion parameters were simultaneously optimized with the selected dynamic model for each spin. The optimized overall correlation time, $\tau_{\rm m}$, was 12.23 ns, the average correlation time of the diffusion tensor ($1/[2D_{\parallel}+4D_{\perp}]$) was 11.96 ns, and the ratio of the principal values of the diffusion tensor ($D_{\parallel}/D_{\perp}$) was 1.39. The associated internal motion parameters are shown in Figs. 6, 7, and 8. The overall correlation time, $\tau_{\rm m}$, and the average correlation time derived from the diffusion tensor, D, showed good agreement (0.27 ns difference). The orientation of the unique axis of the

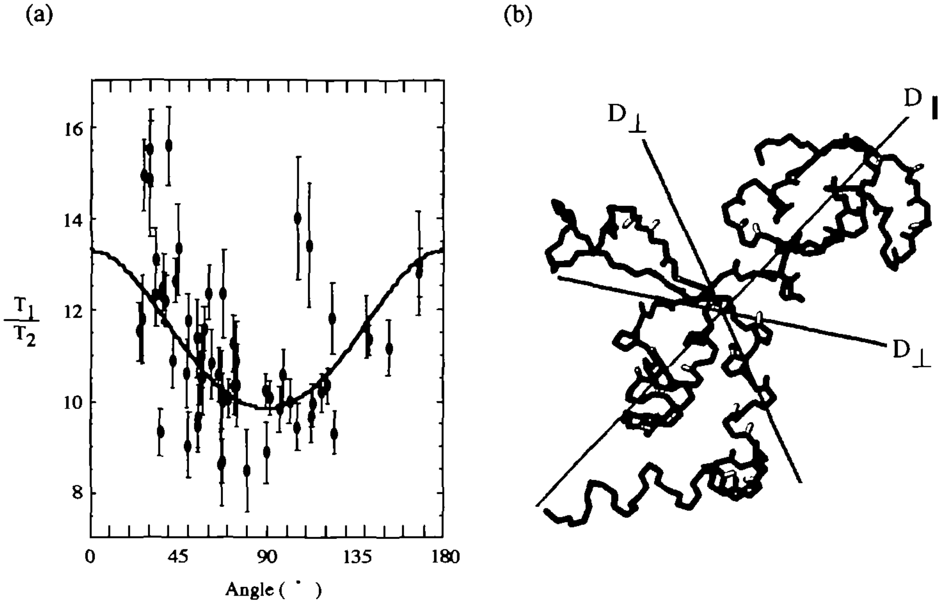

Fig. 5. **Axially symmetric anisotropic character of the rotational diffusion of the central domain of XPA.** (a) Plots of the observed ^{15}N T_1/T_2 ratios at 50.7 MHz against angles, θ, between the NH bond vectors and the unique axis of the diffusion tensor ($D_{\parallel}$) for the coordinates of XPA (PDB: 1xpa). The ^{15}N T_1/T_2 ratios of the spins that showed significant internal motions on a time scale longer than a few hundred picoseconds ($\{^1H\}$-^{15}N NOE<0.65 at 50.7 MHz) or conformational exchange [R_{ex} estimated on $J(0)$ analysis at 50.7 MHz>2.5 s^{-1}] were not used to determine the rotational diffusion tensor, D, and are not plotted in a. The curved line represents the theoretical dependence of the T_1/T_2 ratios on the angle, θ, for the determined diffusion tensor with an anisotropy ($D_{\parallel}/D_{\perp}$) of 1.38 and an average correlation time ($1/[2D_{\parallel}+4D_{\perp}]$) of 12.03 ns. The error bars indicate the $\pm$SD (1σ) values of the uncertainties of the T_1/T_2 ratios. (b) Stick representation of the backbone and NH bonds of the central domain of XPA (PDB: 1xpa) with the principal axis orientations of the determined rotational diffusion tensor, D. Only NH bonds whose coordinates were used to determine the tensor are drawn. The solid lines labeled $D_{\parallel}$ and $D_{\perp}$ correspond to the respective orientations of the tensor elements. The ratio of the lengths of the lines labeled $D_{\parallel}$ and $D_{\perp}$ equals the actual anisotropy of the tensor ($D_{\parallel}/D_{\perp}=1.38$). The orientations of $D_{\perp}$ can be rotated arbitrarily about the unique axis ($D_{\parallel}$) since the tensor, D, is assumed to be axially symmetric. The figure was drawn with the program, MOLMOL (*54*).

TABLE I. **The number of residues selected for each dynamic model on model-free analyses with isotropic and anisotropic rotational diffusion models.**

	Classification[a]						
	Model 1	Model 2	Model 3	Model 4	Model 5	Not fit	Total
Parameters[b]	S^2	S^2,τ_{ef}	S^2,R_{ex}	S^2,τ_{ef},R_{ex}	S_f^2,S^2,τ_{es}		
Isotropic[c]	3[e],2[f],9[g](14)[h]	1,0,0(1)	2,3,9(14)	4,0,15(19)	3,3,21(27)	0,0,15(15)	13,8,69(90)
Anisotropic[d]	5,4,14(23)	4,0,1(5)	0,2,8(10)	3,0,21(24)	None	1,1,23(25)	13,7,67(87)

[a] The five dynamic models applied for fitting in model-free analyses developed by Lipari and Szabo (*36, 37*). [b] The parameters optimized for each dynamic model. [c] Isotropic rotational diffusion was assumed. [d] Axially symmetric anisotropic rotational diffusion was assumed. [e] The number of residues for which only the data (T_1, T_2, and NOE) at the ^{15}N frequency of 50.7 MHz were available and fitted the corresponding dynamic model. [f] The number of residues for which only the data at the ^{15}N frequency of 81.1 MHz were available and fitted the dynamic model. [g] The number of residues for which the data at the ^{15}N frequencies of both 50.7 and 81.1 MHz were available and fitted simultaneously the dynamic model. [h] The sum of the numbers (e), (f), and (g).

diffusion tensor determined on model-free analysis is close to that of the diffusion tensor determined from the T_1/T_2 ratios (6.1° difference), and also close to that of the inertia moment estimated from the molecular coordinates (2.6° difference). The S^2, R_{ex}, and τ_{ef} values determined with the isotropic and anisotropic models showed no statistically significant differences, as described under "DISCUSSION."

Relatively smaller S^2 values (<0.75) were found for residues 130 and 134 in the linker sequence. Significantly smaller S^2 values (<0.6) for the isotropic model were found in parts of loop L1 (residue 158), loop L2 (residues 169, 176, and 177), and the C-terminal region (residues 209, 212, 213, and 215).

DISCUSSION

Description of the Structure—Comparison of the amino acid sequence of the central domain of human XPA with those of XPAs from other eukaryotes, including the yeast homologue of XPA, RAD14, revealed sequence identities ranging from 28% (yeast) to 93% (mouse). The similarity of the tertiary structure of XPA to those of known proteins was analyzed with DALI server version 2.0 (*42*); no previously determined structure with a Z score >1.9 was found in the database.

In the zinc-containing subdomain of XPA, a series of hydrogen bond networks has been found around the four Cys residues: Cys105 NH-Lys110 O, Glu107 NH-Cys105 S_γ, Cys108 NH-Cys105 S_γ, Gly109 NH-Cys105 O, Lys110 NH-Cys108 S_γ, Asn128 NH-Cys126 S_γ, Cys129 NH-Cys126 S_γ, Arg130 NH-Cys126 O, and Cys126 NH-Cys105 S_γ. The presence of these hydrogen bonds is indicated by both the presence of slow exchanging amide protons and structures calculated without these hydrogen bond constraints (*22*). These local structure elements in XPA are common in the $(Cys)_4$ type zinc-fingers of erythroid transcription factor GATA-1 (*43*) and the glucocorticoid receptor (*44, 45*). However, alignment of the zinc-

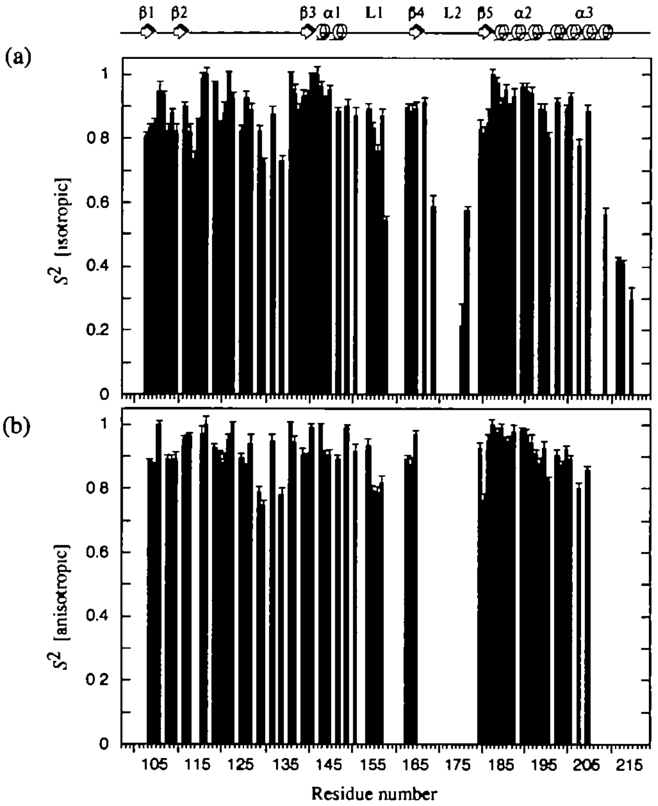

Fig. 6. **Plots of order parameters, S^2, against residue numbers.** The S^2 values were determined on model-free analyses with the isotropic rotational diffusion model (a) and the axially symmetric anisotropic rotational diffusion model (b). For plots a and b, the error bars indicate the ±SD (1σ) values of the uncertainties estimated by Monte Carlo simulations. The secondary structures are indicated at the top.

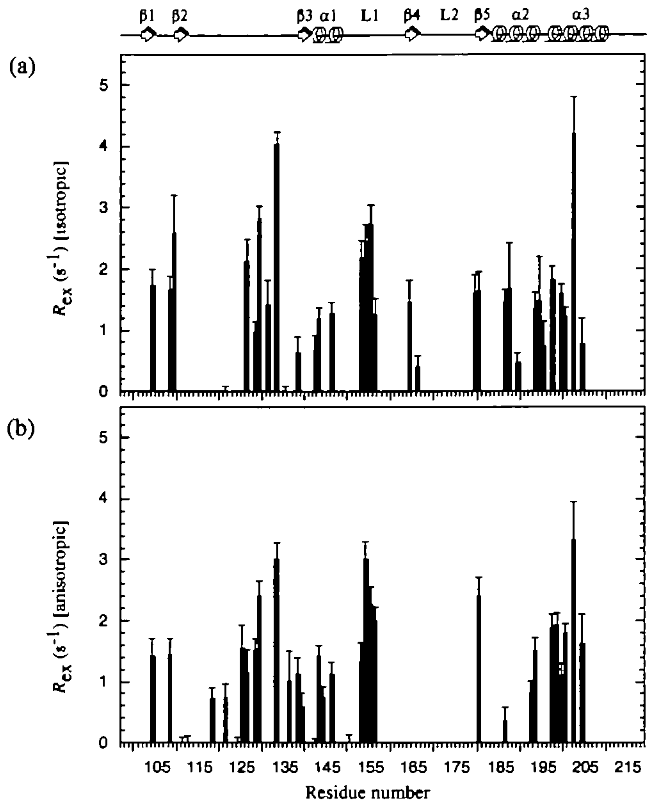

Fig. 7. **Plots of chemical exchange rates, R_{ex}, against residue numbers.** The R_{ex} values were determined on model-free analyses with the isotropic rotational diffusion model (a) and the axially symmetric anisotropic rotational diffusion model (b). For plots a and b, the error bars indicate the ±SD (1σ) values of the uncertainties estimated by Monte Carlo simulations. The secondary structures are indicated at the top.

binding sequence of XPA, Cys-X-X-Cys-$(X)_{17}$-Cys-X-X-Cys, with that of GATA-1 shows that only the positions of the four Cys residues and a Pro residue (XPA position 124) are identical. Moreover, the zinc-finger of GATA-1 has more basic residues than acidic residues, as is usually seen in the zinc-fingers of the DNA binding domains of transcription factors, whereas the zinc-containing subdomain of XPA is highly acidic (Fig. 9a).

Satokata *et al.* have characterized the genomic structure of the human *xpa* gene, and identified six exons in the gene (*46*). Interestingly, the genomic structure of the *xpa* gene shows good correlation to the tertiary structure elements. Exon 3 (residues 96 to 130) encodes the entire zinc-containing subdomain, exon 4 (residues 131 to 185) encodes the linker (residues 130 to 137) and the sheet-helix-loop region (residues 138 to 182), and exon 5 (residues 186 to 224) encodes most of the helix-turn-helix region (residues 183 to 209) and the C-terminal flanking sequence (residues 211 to 219). This indicates that the introns are located at sites corresponding to the inter-module junctions of the central domain of XPA. The correlation between the functional domains of XPA and its genomic structure does not seem to be limited to the central domain. Previous analysis involving truncated XPA showed that a certain region, residues 59 to 97, is necessary for ERCC1 binding, and that this region corresponds almost exactly to the region encoded by exon 2 (residues 58 to 95) (*11, 14-16*). The TFIIH binding site, residues 226 to 273, is encoded by exon 6 (residues 225 to 273) (*12*). Further structural determinations will reveal the relationship between the exons/introns and the tertiary structure elements of these regions (*47, 48*).

Selection of the Diffusion Models—The central domain of XPA consists of a zinc-containing subdomain, a C-terminal subdomain, and a linker sequence connecting the two subdomains (*22*). The relative magnitudes of the inertia moment calculated from the molecular coordinates (PDB: 1xpa) were 1.00:0.90:0.41, indicating that the overall shape of the molecule is rather elliptical. This is consistent with the observation that the T_1/T_2 ratios exhibit wide dispersion, which is due mainly to the anisotropy of the rotational diffusion (Fig. 3c). These observations suggest that an anisotropic diffusion model is preferable for the analysis of the ^{15}N relaxation data.

The F-statistical and random assignment tests have shown that the axially symmetric anisotropic model is more appropriate than the isotropic model for the analysis of the ^{15}N relaxation data. However, we analyzed the relaxation data with the axially symmetric model as well as with the isotropic model for the following two reasons. First, analysis with an axially symmetric model for the ^{15}N spins requires information on the orientations of the corresponding N-H bond vectors. However, this information is not

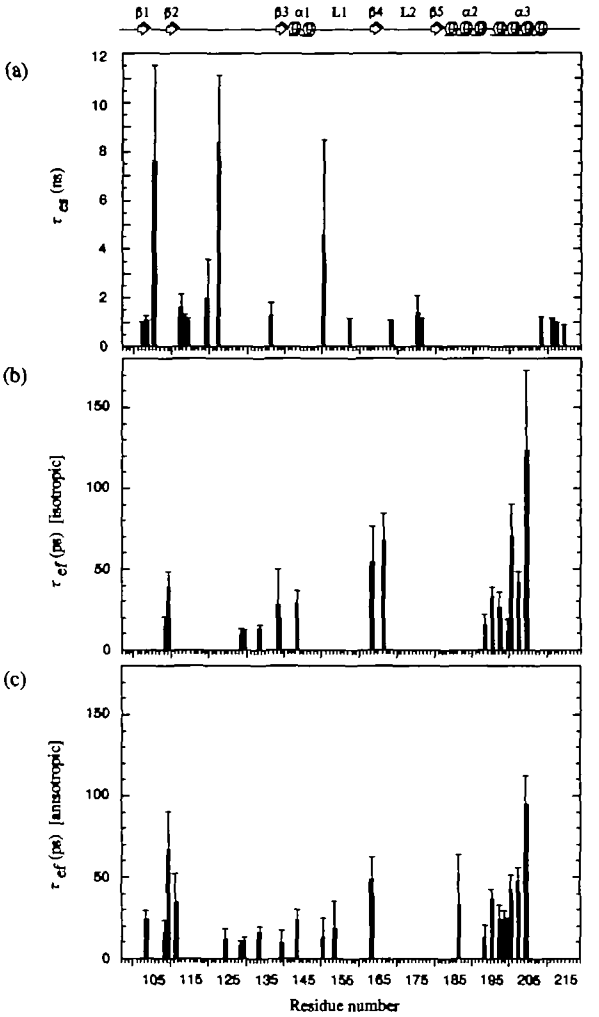

Fig. 8. **Plots of effective correlation times, τ_{ef} and τ_{es}, against residue numbers.** (a) The slow internal correlation times, τ_{es}, were determined on model-free analysis with the isotropic rotational diffusion model using the extended formula for the spectral density function proposed by Clore *et al.* (*38*). This extended formula was not used for model-free analysis with the axially symmetric anisotropic rotational diffusion model. The fast internal correlation times, τ_{ef}, were determined on model-free analyses with the isotropic rotational diffusion model (b) and the axially symmetric anisotropic rotational diffusion model (c). For plots a-c, the error bars indicate the ±SD (1σ) values of the uncertainties estimated by Monte Carlo simulations. The secondary structures are indicated at the top.

available for flexible parts of the molecule, for example, several residues in loop L2. Second, it is generally difficult to distinguish the contribution of overall motional anisotropy from that of slow internal motions (*49*).

Comparison of the Dynamic Parameters—The order parameters, S^2, determined on model-free analyses with the isotropic and axially symmetric anisotropic rotational diffusion models were compared (Fig. 6). The r.m.s. of the differences is 0.050, while the average uncertainties (1σ) of the S^2 values are 0.020 and 0.017 for the isotropic and anisotropic models, respectively. Thus, the S^2 values determined with the two diffusion models do not exhibit statistically significant differences.

Likewise, the chemical exchange rates, R_{ex}, determined on model-free analyses with the isotropic and axially symmetric diffusion models were compared (Fig. 7). The r.m.s. of the differences between the R_{ex} values with the two diffusion models is 0.75 s^{-1}, while the average uncertainties (1σ) of the R_{ex} values are 0.30 s^{-1} and 0.25 s^{-1} for the isotropic and anisotropic models, respectively. This indicates that the R_{ex} values derived with both diffusion models do not exhibit statistically significant differences. Then, R_{ex} values determined on $J(0)$ analysis ($R_{ex\text{-}J0}$) were compared with R_{ex} values determined on model-free analysis ($R_{ex\text{-}mf}$) with the isotropic model (Figs. 4b and 7a). The average difference of the $R_{ex\text{-}J0}$ values from the $R_{ex\text{-}mf}$ values is +0.75 s^{-1}. This positive difference arises mainly from the fact that the $R_{ex\text{-}mf}$ parameter was fixed at zero for dynamic models 1, 2, and 5. However, as the average uncertainty (1σ) of $R_{ex\text{-}J0}$ (0.84 s^{-1}) is comparable to the average difference of +0.75 s^{-1}, the chemical exchange rates determined on the present model-free analyses, $R_{ex\text{-}mf}$, are statistically reliable to the extent of their uncertainties (0.30 s^{-1} and 0.25 s^{-1} for the isotropic and anisotropic models, respectively).

In the similar manner, the fast internal correlation times, τ_{ef}, obtained with the two diffusion models were compared. The r.m.s. of the differences between the τ_{ef} values obtained with the two diffusion models is 10.64 ps, comparable to the average uncertainty (11.37 ps) of the τ_{ef} values, showing that the τ_{ef} values determined with the two diffusion models are statistically similar (Fig. 8).

On model-free analysis with the isotropic diffusion model, model 5 was incorporated into the model selection, which includes effective correlation times for slow internal motions, τ_{es}, in addition to the overall correlation time, τ_m. On the other hand, for analysis with the anisotropic rotational diffusion model, model 5 was not included in the model selection procedure because it has recently been shown that slow internal correlation times in an isotropic diffusion model often originate from an anisotropy of the overall rotational diffusion (*49*). Out of the 27 spins assigned to model 5 in the isotropic model, 13 were fitted reasonably well to any of models 1 to 4 in the anisotropic model; only two could be fitted when the additional parameter, τ_{es}, was added (model 5), and the remaining 12 spins could not be assigned to any of the dynamic models with the anisotropic model, probably because the orientations of the amide bonds for these 12 spins are not fixed rigidly (average $\{^1H\}$-^{15}N NOE value, 0.61 at 50.7 MHz). These results suggest that the slow internal motions of about half of these 27 spins determined with the isotropic model may originate from the overall anisotropic motion, and the rest of the spins may actually have slow internal motions.

Backbone Dynamics and Their Implications for Biological Function—Uniformly high order parameter, S^2, values are observed for the zinc-containing subdomain, except for N-terminal residues 98 to 103, suggesting that this region is among the most rigid ones in the protein molecule. This feature is probably due to the stabilization of the subdomain by the zinc coordination with the associated extensive hydrogen bond networks, and the hydrophobic core formed by residues V103, F112, and M118 (*22*).

Small $\{^1H\}$-^{15}N NOE values (<0.55 at 50.7 MHz), large T_2 values, and small S^2 values (<0.6) are characteristic of a part of loop L1 (residues 158), a part of loop L2 (residues 168 to 179), the latter half of helix $\alpha 3$, and the following

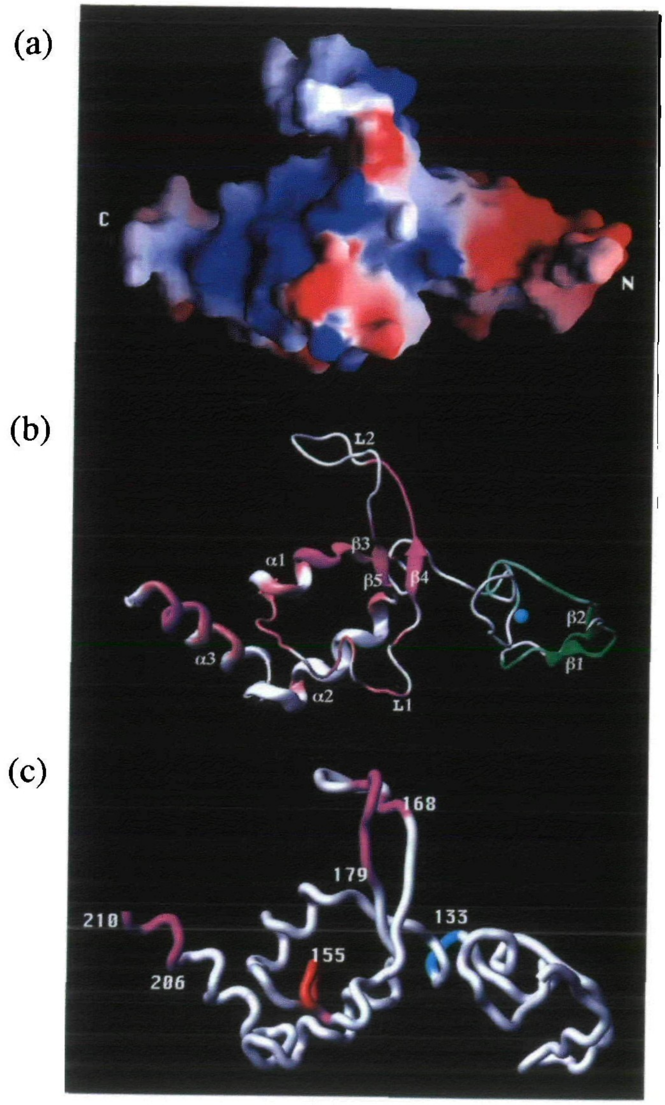

Fig. 9. **Mapping of the electrostatic potential, interaction surfaces, and flexible regions of XPA.** (a) Distribution of the electrostatic potential, displayed with GRASP (*55*), on the solvent-accessible surface of the central domain of XPA (residues 98 to 210) (*22*). Blue corresponds to positive potential and red to negative potential. The presence of a positively charged cleft is evident in the C-terminal subdomain. In the zinc-containing subdomain, negatively charged patches are dominant. The molecular orientation is the same as in b. (b) Mapping of the XPA residues with chemical shift perturbations or broadening effects in the ^{15}N-^{1}H-HSQC spectra obtained previously (*22*). The residues showing perturbed amide resonances upon complex formation with the cisplatin-damaged 24-mer oligonucleotide are indicated in magenta, and the residues showing specifically broadened amide resonances upon complex formation with RPA70$_{181\text{-}422}$ are colored green. (c) Mapping of the flexible parts of XPA that are related to its function. Regions exhibiting internal motions on a picosecond to nanosecond time scale characterized by small {^{1}H}-^{15}N NOE values (<0.55 at 50.7 MHz), large T_2 values, small S^2 values (<0.6), slow internal correlation times on the order of 1 ns, and little contribution from R_{ex} values are drawn in magenta (residues 158, 168 to 179, and 206 to 218). A region exhibiting conformational exchange on a microsecond to millisecond time scale characterized by large R_{ex} values (>2.0 s^{-1} at 50.7 MHz) is drawn in red (residues 154 to 157). These regions are located in the interaction surface for DNA. Residues 133 and 134 with large R_{ex} values (>3.5 s^{-1} at 50.7 MHz) are drawn in cyan. This region serves as a linker connecting the zinc-containing subdomain and the C-terminal subdomain, and exhibits conformational exchange on a microsecond to millisecond time scale. The figures in b and c were drawn with the program, MOLMOL (*54*).

C-terminal region (residues 206 to 218), suggesting that these regions are not rigid but exhibit a large extent of mobility. These regions show contributions from slow internal correlation times, τ_{es}, of an order of 1 ns on model-free analysis with the isotropic diffusion model, but show no significant contributions from the R_{ex} values. These observations suggest that these regions exhibit internal motions on a picosecond to nanosecond time scale. On the other hand, larger R_{ex} values (>2.0 s^{-1} at 50.7 MHz) were observed for a part of loop L1 (residues 154 to 157), indicating the presence of conformational exchange on a microsecond to millisecond time scale. All these regions that exhibit picosecond to nanosecond motions or microsecond to millisecond motions are exposed to solvent and are parts of the DNA binding surface, as suggested by the previous chemical shift perturbation experiment (*22*) (Fig. 9). The internal motions of these regions may play a role in the interaction of the central domain of XPA with various kinds of damaged DNA by altering the conformation of the interaction surface to fit the structures of damaged DNAs. High rates of amide proton exchange are also observed in these regions, suggesting that conformational exchange of large magnitude on a slower time scale is also possible. The previous filter binding experiments showed the affinities of the central domain of XPA for 2,686 bp DNAs with and without multiple damages (*8*). According to our calculation based on these results, the dissociation constant, K_d, for XPA$_{98\text{-}219}$ and DNA damaged by UV or cisplatin is approximately 4×10^{-8} M, and the K_d for XPA$_{98\text{-}219}$ and the non-damaged DNA is in the range of 3×10^{-6} to 6×10^{-7} M.

The average T_1/T_2 ratio for the zinc-containing subdomain was almost the same as the average T_1/T_2 ratio for the C-terminal subdomain (Fig. 3c), showing that the two subdomains undergo rotational diffusion with similar correlation times (*50*). The hydrophobic core formed between residues Y116, L117, F121, and L123 in the zinc-containing subdomain, and residues L138, I165, L182, and L184 in the C-terminal subdomain, possibly restricts the independent motion of each subdomain. The ^{15}N spins of residues 133 and 134 located in the linker sequence have large R_{ex} values (>3.5 s^{-1} at 50.7 MHz), showing that the linker sequence may exhibit conformational exchange on a microsecond to millisecond time scale (Fig. 9c).

NER is a major DNA repair pathway whose mechanism is highly conserved. However, the three-dimensional structures of only the central domain of human XPA (*22*) and the single-stranded-DNA-binding domain of RPA70 (*51*) are known for proteins involved in the early steps of NER. We have shown the resonance assignments of most of the ^{1}H, ^{13}C, and ^{15}N spins of the central domain of human XPA.

From the analysis of the ^{15}N relaxation data, we found that the rotational diffusion of the central domain of XPA has an anisotropic character. Thus, we applied an anisotropic rotational diffusion model as well as an isotropic model for model-free analyses of the ^{15}N relaxation data to obtain parameters for the internal motions of the backbone and the overall rotational diffusion of the domain. As a result, we have shown that the internal motion parameters, obtained with the isotropic model and the anisotropic model, are similar except for the parameters for the slow internal motions of nanosecond order. The large values of these slow internal motions determined on model-free analysis with the isotropic model may arise from the overall anisotropic motion.

The previous RPA- and DNA-binding experiments suggested that the acidic zinc-containing subdomain and the basic cleft in the C-terminal subdomain are involved in the binding to RPA70 and DNA, respectively (*22*). Interestingly, the surface of the cleft contains most of the flexible regions identified on analyses of the relaxation data, while the zinc-containing subdomain is completely rigid. XPA recognizes structurally unrelated DNA damage such as (6-4) photoproducts and crosslinks caused by UV and chemicals like cisplatin and osmium-tetroxide (*8*). The flexibility of these regions may be important for the interactions of XPA with various kinds of damaged DNA.

We wish to thank Drs. E.H. Morita, M. Shimizu, T. Shimizu, M. Maeda, Y.J. Ping, Y.H. Jeon, and M. Wälchli for helpful discussions. We would also like to thank Dr. A.G. Palmer III for providing MODELFREE-4.0. The coordinates have been deposited in the Brookhaven Protein Data Bank as *1xpa*. Other NMR data (chemical shifts, coupling constants, and distance and angle constraints) have been deposited in the BioMagResBank as *r1xpamr*.

REFERENCES

1. Aboussekhra, A. and Wood, R.D. (1994) Repair of UV-damaged DNA by mammalian cells and *Saccharomyces cerevisiae*. *Curr. Opin. Genet. Dev.* **4**, 212-220
2. Cleaver, J.E. and Kraemer, K.H. (1995) Xeroderma pigmentosum in *The Metabolic Basis of Inherited Disease*, 7th Ed. (C.R. Scriver *et al.*, eds.) pp. 4393-4419, McGraw-Hill, New York
3. Hoeijmakers, J.H. and Bootsma, D. (1990) Molecular genetics of eukaryotic DNA excision repair. *Cancer Cells Mon. Rev.* **2**, 311-320
4. Tanaka, K. *et al.* (1990) Analysis of a human DNA excision repair gene involved in group A xeroderma pigmentosum and containing a zinc-finger domain. *Nature* **348**, 73-76
5. Robins, P., Jones, C.J., Biggerstaff, M., Lindahl, T., and Wood, R.D. (1991) Complementation of DNA repair in xeroderma pigmentosum group A cell extracts by a protein with affinity for damaged DNA. *EMBO J.* **10**, 3913-3921
6. Jones, C.J. and Wood, R.D. (1993) Preferential binding of the xeroderma pigmentosum group A complementing protein to damaged DNA. *Biochemistry* **32**, 12096-12104
7. Asahina, H. *et al.* (1994) The XPA protein is a zinc metalloprotein with an ability to recognize various kinds of DNA damage. *Mutat. Res.* **315**, 229-237
8. Kuraoka, I., Morita, E.H., Saijo, M., Matsuda, T., Morikawa, K., Shirakawa, M., and Tanaka, K. (1996) Identification of a damaged-DNA binding domain of the XPA protein. *Mutat. Res.* **362**, 87-95
9. He, Z., Henricksen, L.A., Wold, M.S., and Ingles, C.J. (1995) RPA involvement in the damage-recognition and incision steps of nucleotide excision repair. *Nature* **374**, 566-569
10. Li, L., Lu, X., Peterson, C.A., and Legerski, R.J. (1995) An interaction between the DNA repair factor XPA and replication protein A appears essential for nucleotide excision repair. *Mol. Cell. Biol.* **15**, 5396-5402
11. Saijo, M., Kuraoka, I., Masutani, C., Hanaoka, F., and Tanaka, K. (1996) Sequential binding of DNA repair proteins RPA and ERCC1 to XPA *in vitro*. *Nucleic Acids Res.* **24**, 4719-4724
12. Park, C.-H., Mu, D., Reardon, J.T., and Sancar, A. (1995) The general transcription-repair factor TFIIH is recruited to the excision repair complex by the XPA protein independent of the TFIIE transcription factor. *J. Biol. Chem.* **270**, 4896-4902
13. Nocentini, S., Coin, F., Saijo, M., Tanaka, K., and Egly, J.-M. (1997) DNA damage recognition by XPA protein promotes efficient recruitment of transcription factor II H. *J. Biol. Chem.* **272**, 22991-22994
14. Li, L., Elledge, S.J., Peterson, C.A., Bales, E.S., and Legerski, R.J. (1994) Specific association between the human DNA repair proteins XPA and ERCC1. *Proc. Natl. Acad. Sci. USA* **91**, 5012-5016
15. Li, L., Peterson, C.A., Lu, X., and Legerski, R.J. (1995) Mutations in XPA that prevent association with ERCC1 are defective in nucleotide excision repair. *Mol. Cell. Biol.* **15**, 1993-1998
16. Nagai, A. *et al.* (1995) Enhancement of damage-specific DNA binding of XPA by interaction with the ERCC1 DNA repair protein. *Biochem. Biophys. Res. Commun.* **211**, 960-966
17. Mu, D., Hsu, D.S., and Sancar, A. (1996) Reaction mechanism of human DNA repair excision nuclease. *J. Biol. Chem.* **271**, 8285-8294
18. Wakasugi, M. and Sancar, A. (1998) Assembly, subunit composition, and footprint of human DNA repair excision nuclease. *Proc. Natl. Acad. Sci. USA* **95**, 6669-6674
19. Sugasawa, K., Ng, J.M., Masutani, C., Iwai, S., van der Spek, P.J., Eker, A.P., Hanaoka, F., Bootsma, D., and Hoeijmakers, J.H. (1998) Xeroderma pigmentosum group C protein complex is the initiator of global genome nucleotide excision repair. *Mol. Cell* **2**, 223-232
20. Morita, E.H., Ohkubo, T., Kuraoka, I., Shirakawa, M., Tanaka, K., and Morikawa, K. (1996) Implications of the zinc-finger motif found in the DNA-binding domain of the human XPA protein. *Genes Cells* **1**, 437-442
21. Miyamoto, I., Miura, N., Niwa, H., Miyazaki, J., and Tanaka, K. (1992) Mutational analysis of the structure and function of the xeroderma pigmentosum group A complementing protein. Identification of essential domains for nuclear localization and DNA excision repair. *J. Biol. Chem.* **267**, 12182-12187
22. Ikegami, T., Kuraoka, I., Saijo, M., Kodo, N., Kyogoku, Y., Morikawa, K., Tanaka, K., and Shirakawa, M. (1998) Solution structure of the DNA- and RPA-binding domain of the human repair factor XPA. *Nat. Struct. Biol.* **5**, 701-706
23. Buchko, G.W., Ni, S., Thrall, B.D., and Kennedy, M.A. (1997) Human nucleotide excision repair protein XPA: expression and NMR backbone assignments of the 14.7 kDa minimal damaged DNA binding domain (Met98-Phe219). *J. Biomol. NMR* **10**, 313-314
24. Buchko, G.W., Ni, S., Thrall, B.D., and Kennedy, M.A. (1998) Structural features of the minimal DNA binding domain (M98-F219) of human nucleotide excision repair protein XPA. *Nucleic Acids Res.* **26**, 2779-2788
25. Hess, N.J., Buchko, G.W., Conradson, S.D., Espinosa, F.J., Ni, S., Thrall, B.D., and Kennedy, M.A. (1998) Human nucleotide excision repair protein XPA: extended X-ray absorption fine-structure evidence for a metal-binding domain. *Protein Sci.* **7**, 1970-1975
26. Cavanagh, J., Fairbrother, W.J., Palmer III, A.G., and Skelton, N.J. (1996) *Protein NMR Spectroscopy*, Academic Press, San Diego
27. Clore, G.M. and Gronenborn, A.M. (1993) *NMR of Proteins*, Macmillan, London
28. Hu, W. and Zuiderweg, E.R.P. (1996) Stereospecific assignments of Val and Leu methyl groups in a selectively ^{13}C-labeled 18 kDa polypeptide using 3D CT-(H)CCH-COSY and 2D $^1J_{C\text{-}C}$ edited heteronuclear correlation experiments. *J. Magn. Reson. B* **113**, 70-75
29. Farrow, N.A., Muhandiram, R., Singer, A.U., Pascal, S.M., Kay, C.M., Gish, G., Shoelson, S.E., Pawson, T., Forman-Kay, J.D., and Kay, L.E. (1994) Backbone dynamics of a free and a phosphopeptide-complexed src homology 2 domain studied by ^{15}N NMR relaxation. *Biochemistry* **33**, 5984-6003
30. Delaglio, F., Grzesiek, S., Vuister, G.W., Zhu, G., Pfeifer, J., and

Bax, A. (1995) NMRPipe: a multidimensional spectral processing system based on UNIX pipes. *J. Biomol. NMR* **6**, 277-293

31. Garrett, D.S., Powers, R., Gronenborn, A.M., and Clore, G.M. (1991) A common sense approach to peak picking in two-, three, and four-dimensional spectra using automatic computer analysis of contour diagrams. *J. Magn. Reson.* **95**, 214-220
32. Mandel, A.M., Akke, M., and Palmer, III A.G. (1995) Backbone dynamics of *Escherichia coli* ribonuclease HI: correlations with structure and function in an active enzyme. *J. Mol. Biol.* **246**, 144-163
33. Bevington, P.R. and Robinson, D.K. (1992) *Data Reduction and Error Analysis for the Physical Sciences*, 2nd ed., pp. 38-52, 161-164, McGraw-Hill, New York
34. Peng, J.W. and Wagner, G. (1995) Frequency spectrum of NH bonds in eglin c from spectral density mapping at multiple fields. *Biochemistry* **34**, 16733-16752
35. Wong, K.-B., Fersht, A.R., and Freund, S.M.V. (1997) NMR ^{15}N relaxation and structural studies reveal slow conformational exchange in barstar C40/82A. *J. Mol. Biol.* **268**, 494-511
36. Lipari, G. and Szabo, A. (1982) Model-free approach to the interpretation of nuclear magnetic resonance relaxation in macromolecules. 1. Theory and range of validity. *J. Am. Chem. Soc.* **104**, 4546-4559
37. Lipari, G. and Szabo, A. (1982) Model-free approach to the interpretation of nuclear magnetic resonance relaxation in macromolecules. 2. Analysis of experimental results. *J. Am. Chem. Soc.* **104**, 4559-4570
38. Clore, G.M., Szabo, A., Bax, A., Kay, L.E., Driscoll, P.C., and Gronenborn, A.M. (1990) Deviations from the simple two-parameter model-free approach to the interpretation of nitrogen-15 nuclear magnetic relaxation of proteins. *J. Am. Chem. Soc.* **112**, 4989-4991
39. Tjandra, N., Wingfield, P., Stahl, S., and Bax, A. (1996) Anisotropic rotational diffusion of perdeuterated HIV protease from ^{15}N NMR relaxation measurements at two magnetic fields. *J. Biomol. NMR* **8**, 273-284
40. Woessner, D.E. (1962) Nuclear spin relaxation in ellipsoids undergoing rotational Brownian motion. *J. Chem. Phys.* **37**, 647-654
41. Wishart, D.S. and Sykes, B. (1994) Chemical shifts as a tool for structure determination in *Methods in Enzymology* (James, T.L. and Oppenheimer, N.J., eds.) Vol. 239, pp. 363-392, Academic Press, San Diego
42. Holm, L. and Sander, C. (1993) Protein structure comparison by alignment of distance matrices. *J. Mol. Biol.* **233**, 123-138
43. Omichinski, J.G. *et al.* (1993) NMR structure of a specific DNA complex of Zn-containing DNA binding domain of GATA-1. *Science* **261**, 438-446
44. Luisi, B.F., Xu, W.X., Otwinowski, Z., Freedman, L.P., Yamamoto, K.R., and Sigler, P.B. (1991) Crystallographic analysis of the interaction of the glucocorticoid receptor with DNA. *Nature* **352**, 497-505
45. Summers, M.F. (1996) Zinc fingers in *Encyclopedia of Nuclear Magnetic Resonance* (Grant, D.M. and Harris, R.K., eds.) pp. 5063-5071, John Wiley and Sons, West Sussex, England
46. Satokata, I., Iwai, K., Matsuda, T., Okada, Y., and Tanaka, K. (1993) Genomic characterization of the human DNA excision repair-controlling gene XPAC. *Gene* **136**, 345-348
47. Go, M. (1985) Protein structures and split genes. *Adv. Biophys.* **19**, 91-131
48. Nakashima, T. *et al.* (1994) Structure of the human CCG1 gene: relationship between the exons/introns and functional domain/modules of the protein. *Gene* **141**, 193-200
49. Schurr, J.M., Babcock, H.P., and Fujimoto, B.S. (1994) A test of the model-free formulas. Effects of anisotropic rotational diffusion and dimerization. *J. Magn. Reson. B* **105**, 211-224
50. Zhou, H., McEvoy, M.M., Lowry, D.F., Swanson, R.V., Simon, M.I., and Dahlquist, F.W. (1996) Phosphotransfer and CheY-binding domains of the histidine autokinase CheA are joined by a flexible linker. *Biochemistry* **35**, 433-443
51. Bochkarev, A., Pfuetzner, R.A., Edwards, A.M., and Frappier, L. (1997) Structure of the single-stranded-DNA-binding domain of replication protein A bound to DNA. *Nature* **385**, 176-181
52. Kraulis, P.J. (1991) MOLSCRIPT: a program to produce both detailed and schematic plots of protein structures. *J. Appl. Crystallogr.* **24**, 946-950
53. Merritt, E.A. and Bacon, D.J. (1997) Raster3D photorealistic molecular graphics. *Methods Enzymol.* **277**, 505-524
54. Koradi, R., Billeter, M., and Wüthrich, K. (1996) MOLMOL: a program for display and analysis of macromolecular structures. *J. Mol. Graph.* **14**, 51-55
55. Nicholls, A., Sharp, K.A., and Honig, B. (1991) Protein folding and association: insights from the interfacial and thermodynamic properties of hydrocarbons. *Proteins Struct. Funct. Genet.* **11**, 281-296